



ARTICLE

The Turbulent Schmidt Number for Transient Contaminant Dispersion in a Large Ventilated Room Using a Realizable $k-\epsilon$ Model

Fei Wang, Qinpeng Meng, Jinchi Zhao, Xin Wang, Yuhong Liu and Qianru Zhang*

School of Environment and Architecture, University of Shanghai for Science and Technology, Shanghai, 200093, China

*Corresponding Author: Qianru Zhang. Email: zhangqianru@usst.edu.cn

Received: 02 October 2022 Accepted: 20 October 2023 Published: 28 March 2024

ABSTRACT

Buildings with large open spaces in which chemicals are handled are often exposed to the risk of explosions. Computational fluid dynamics is a useful and convenient way to investigate contaminant dispersion in such large spaces. The turbulent Schmidt number (Sc_t) concept has typically been used in this regard, and most studies have adopted a default value. We studied the concentration distribution for sulfur hexafluoride (SF_6) assuming different emission rates and considering the effect of Sc_t . Then we examined the same problem for a light gas by assuming hydrogen gas (H_2) as the contaminant. When SF_6 was considered as the contaminant gas, a variation in the emission rate completely changed the concentration distribution. When the emission rate was low, the gravitational effect did not take place. For both low and high emission rates, an increase in Sc_t accelerated the transport rate of SF_6 . In contrast, for H_2 as the contaminant gas, a larger Sc_t could induce a decrease in the H_2 transport rate.

KEYWORDS

Large space; CFD; turbulent Schmidt number; contaminant dispersion; emission rate

Nomenclature

Sc_t	Turbulent Schmidt number
ρ	Density of the fluid
φ	Scalar
t	Time
\vec{U}	Velocity vector
Γ_φ	Diffusion coefficient
S_φ	Source term
μ_t	Turbulent viscosity
D_t	Turbulent diffusivity
u_i	Velocity in the i th direction
μ	Dynamic viscosity
λ	Thermal conductivity
d	Diffusion coefficient for the species in the mixture
C_p	Specific heat at constant pressure
T	Temperature
Y_i	Mass fraction of the i th species



P	Pressure
c	Concentration
Q	Thermal energy
Q_m	Source emission rate
g	Gravitational acceleration
k	Turbulence kinetic energy
ε	Rate of dissipation for turbulence kinetic energy
G_k	Generation of turbulence kinetic energy due to the mean velocity gradients
G_b	Generation of turbulence kinetic energy due to buoyancy
Y_M	Contribution of the fluctuating dilatation in compressible turbulence to the overall dissipation rate
$C_{1\varepsilon}$	Constant
$C_{2\varepsilon}$	Constant
$C_{3\varepsilon}$	Constant
σ_k	Turbulent Prandtl number for k
σ_ε	Turbulent Prandtl number for ε
S_k	User-defined source term
S_ε	user-defined source term
C_μ	Constant
C	The concentration of SF ₆
C_0	Contaminant concentration when the room is fully mixed
q	Contaminant emission rate
Q_v	Room ventilation rate

1 Introduction

Environmental risk assessment is often associated with open areas due to the accidents that occur in chemical processing installations, which are built in such areas. Many researchers have focused on dense gas dispersion in the atmospheric environment and have proposed theoretical models to solve the dense gas dispersion problem [1–4]. Nevertheless, there are still exist accidental release of a sustained, small, undetected leak of a dense toxic gas (chlorine) in an industrial indoor environment in which the risk posed by the indoor handling of chemicals must be assessed [5].

With the development of computational fluid dynamics (CFD), an increasing number of studies have used simulation [6]. The turbulent Schmidt number (Sc_t) is a necessary parameter in the simulation of gas dispersion in ventilated rooms. Sc_t was proposed to calculate turbulent diffusivity:

$$Sc_t = \frac{\mu_t}{D_t}$$

After comparing simulations with experimental data, Spalding [7] recommended an Sc_t value of 0.7. As Bady et al. [8] pointed out, however, Sc_t is not constant and varies from one location to another within the same calculation domain. Tahmooreesi et al. [9] simulated seven scenarios with different values of Sc_t , and the results showed that changing the turbulent Schmidt number has significant consequences for mixing and geometrical parameters. Balestrin et al. [10] presented an alternative to better predict turbulent catalytic systems with surface reaction limited by mass transfer selecting an optimal turbulent Schmidt number (Sc_t varying from 0.2 to 1.1). Other researchers have conducted studies related to different Sc_t value [11–13].

When studying Sc_t , knowledge of the turbulent diffusivity is required. Based on the analogy between the exchange of mass and momentum, the turbulent viscosity (momentum) is usually used instead of the

turbulent diffusivity of mass [14]. The specific Sc_t has a significant effect on the prediction results [15]. Most researchers have assumed Sc_t to be a constant.

Within the study of the atmosphere, it is recommended that Sc_t be determined by considering the dominant flow structure in each case, and Tominaga et al. [15] classified the literature into categories accordingly. In the jet-in-crossflow field, He et al. [16] gave the Sc_t expression along the jet and proved that Sc_t is a variable instead of a constant in a simulation based on Kamotani et al. [17] velocity and temperature trajectories. They also studied species spreading in jet-in-crossflow with different momentum ratios between the jet and the crossflow. An Sc_t of 0.2 was recommended for optimal agreement with the experimental data. However, as remarked in Tominaga et al. [15], the predicted turbulence intensity around the jet given by this computation is underestimated in comparison with the experiment, which can be compensated for in this case by the large Sc_t . If this assumption is correct, the optimum value of 0.2 recommended in that study is indeed very low. In the dispersion in boundary layers, the optimum Sc_t is widely distributed in the range of 0.2–1.3 in the atmospheric dispersion field [15]. Koeltzsch [14] conducted wind tunnel experiments of the flow above a plate and demonstrated that, within the boundary layer, Sc_t has a strong dependence on height. By fitting the experimental data, a power series was proposed to calculate the Sc_t in the boundary layer. In regard to plume dispersion in the boundary layer, a smaller Sc_t value is supposed to increase the turbulent diffusion near the ground. For concentrations around plumes in open country and around a single building, a smaller value of Sc_t such as 0.3 tends to provide more accurate predictions of concentration distribution. A smaller value of Sc_t can compensate for the underestimation of the turbulent diffusion for momentum. In Tominaga et al. [15], other types of flows were also investigated. For turbidity currents, for example, the authors recommend a higher value of Sc_t . As Gromke et al. [18] state, the Sc_t in a given flow field is spatially variable. It is a fitting parameter that depends on the mean and turbulent characteristics of a flow field, on the position(s) and type(s) of the pollutant source(s), and on the abundance and the heterogeneity of the distribution of the pollutant species in space. They used four normalized merits to judge the Sc_t for pollutant dispersion simulations in an urban neighborhood, with an Sc_t value of 0.5.

Few studies, however, have investigated Sc_t in the pollutant dispersion in indoor simulations. Moreover, most researchers use a constant Sc_t , as summarized in Table 1.

Table 1: Sc_t in indoor contaminant dispersion

Author	Year	Sc_t
Siddiqui et al. [5]	2012	Close to unity
Nagaosa [19]	2014	1
Cao et al. [20]	2013	0.9
Dong et al. [21]	2017	0.7
Marquardt et al. [22]	2020	0.7

Table 1 shows that, when researchers modified the default value of Sc_t (0.7), they usually changed it to 1 or 0.9. Shi et al. [23] introduced a new dynamic Sc_t model for the simulation of stratified flows. Li et al. [24] proposed another Schmidt number model for contaminant dispersion in an indoor environment. These two studies share a similar procedure, namely to calibrate the models with two experimental conditions using two levels of the dimensionless numbers to obtain the constant values. The objects are different, however. In Shi et al. [23], the object is the stratified flow, and the dimensionless number is the Richardson number. In Li et al. [24], the researchers assumed that indoor contaminant dispersion is related to the vortex structures and thus the dimensionless number is the Okubo–Weiss Q value.

In summary, under indoor pollutant dispersion simulation, Sc_t is a necessary parameter for calculating turbulent diffusivity, and many researchers set it as a default value in the simulation, but this is not very rigorous, each pollutant has different effects on Sc_t , and modifying Sc_t arbitrarily may have a large impact on the simulation results. In this paper, SF_6 with high density and H_2 with low density are selected as research objects to explore their effects on Sc_t , and the conclusions can play a certain guiding role for the subsequent researchers to conduct numerical simulations.

2 Experimental Setup

2.1 Experimental Chamber

A $5 \times 6 \times 6$ (length, width, height in meters) chamber was constructed with a steel frame and glass, as shown in Fig. 1. Good airtightness was assumed.



Figure 1: Overview of the chamber

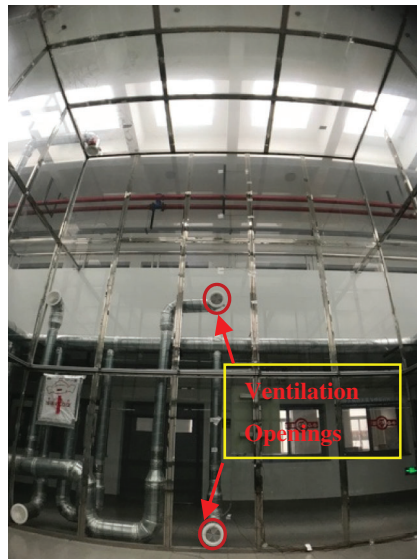
Note: Figure source: Zhang et al. [25].

Two ventilation openings were chosen to perform the air distribution, as shown in Figs. 2a and 2b, which are located in the middle and bottom of the wall. Both grilles have a diameter of 165mm, and the effective area ratio is 53.3%. The grilles locations are illustrated in Fig. 2b.

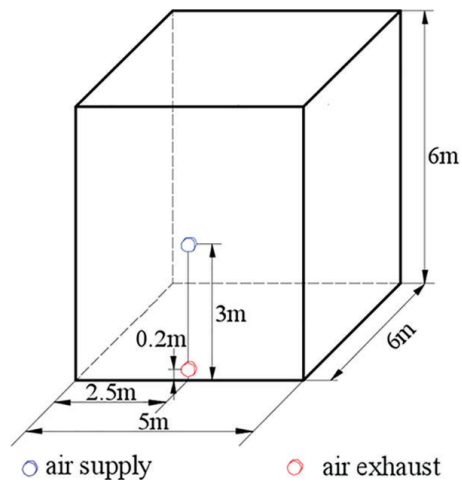
The photoacoustic gas monitor (0–500 ppm \pm 3%, INNOVA 1412i) was connected to the pipes to record the test point concentration, and the contaminant gas was released at a set point. Anemometers (0.05–30 m/s \pm 0.05 m/s) were used to record the velocity at several places. The samplers are depicted in Fig. 3.

The contaminant source position and the measure point positions are presented in Fig. 4. In each of the experiments, the contaminant source is located at A or B (3 or 1 m from the floor).

The contaminant point source was modeled by a table tennis ball on which was uniformly distributed 288 holes of 0.5 mm diameter, as shown in Fig. 5. More details of the experiments can be found in Zhang et al. [25].



(a) The two grilles used in this study.



(b) Diagram of the chamber.

Figure 2: Diagram of the lab and positions of the ventilation openings

Note: Figure source: Zhang et al. [25].

2.2 Validation Conditions

Several ventilation conditions were analyzed in Zhang et al. [25]. One of the experiments was chosen as the benchmark for this study, as shown in Table 2. In that experiment, the air was supplied from the middle opening and exhausted from the bottom. The air change rate was 3 h^{-1} , and the contaminant source rate was 3 mL/s , which was located at A (3 m above the floor).



Figure 3: Contaminant sampler and anemometer head
 Note: Figure source: Zhang et al. [25].

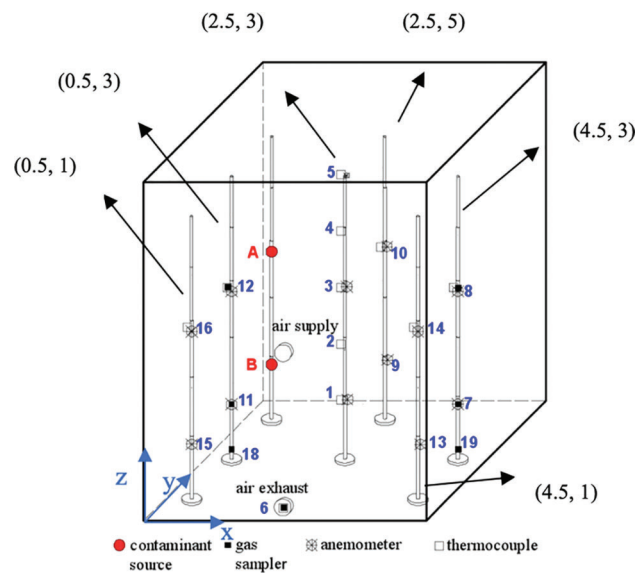


Figure 4: Measurement points in the experimental chamber
 Note: Figure source: Zhang et al. [25].



Figure 5: The contaminant point source

Note: Figure source: Zhang et al. [25].

Table 2: Dependent variables, effective diffusion coefficients, and the source terms in the transport equation

Equation	φ	Γ_{φ}	S_{φ}
Continuity	1	0	0
Momentum X	u	μ	$-\frac{\partial P}{\partial x}$
Momentum Y	v	μ	$-\frac{\partial P}{\partial y}$
Momentum Z	w	μ	$-\frac{\partial P}{\partial z} - g\rho$
Energy	$C_p T$	λ	Q (0W)
Concentration	Y_i	d	Q_m (3 mL/s)

3 Computational Setup

3.1 Numerical Methods

The ANSYS Fluent was used for the transient Reynolds-averaged Navier–Stokes (RANS) computations based on a control volume approach for solving flow and mass fraction equations. The Green–Gauss cell-based scheme was used for gradient discretization. The advection terms were discretized using a second-order upwind scheme. The semi-implicit method for the pressure-linked equation (SIMPLE) algorithm was used for the pressure-velocity coupling. The spatial discretization for the gradient was least squares cell-based by default and for pressure altered to standard. The rest of the spatial discretization was all set to second-order upwind.

The spatial distribution of airflow, temperature, and species in the zone is governed by the conservation laws of mass, momentum, and energy. The governing advection–diffusion equations of the fluid are all in the following form [26,27]:

$$\frac{\partial \rho \phi}{\partial t} + \text{div}(\rho \vec{U} \phi) = \text{div}(\Gamma_{\phi} \overrightarrow{\text{grad}} \phi) + S_{\phi} \quad (1)$$

The dependent variables, effective diffusion coefficients, and the source terms for each equation are presented in Table 2.

In ANSYS Fluent, the local mass fraction of the species, Y_i , was calculated by solving a convection–diffusion equation for the species with the parameter in the last row of Table 2.

3.2 Domains and Computational Grid

The indoor airflow was generated by the jet at the inlet and the flow at the source. Because the chamber was large compared with the inlet opening, a large pressure gradient occurred. Near the jet, a large pressure gradient existed because of the high inlet velocity and the small environment velocity. Near the source, the source velocity was small compared with the environment velocity; the concentration gradient was substantial at the outlet. Thus, close to the air inlet and the contaminant source, fine grids were employed.

The general idea was to create three zones, denominated as JET_ZONE, SOURCE_ZONE, and BODY_ZONE, as shown in Fig. 6.

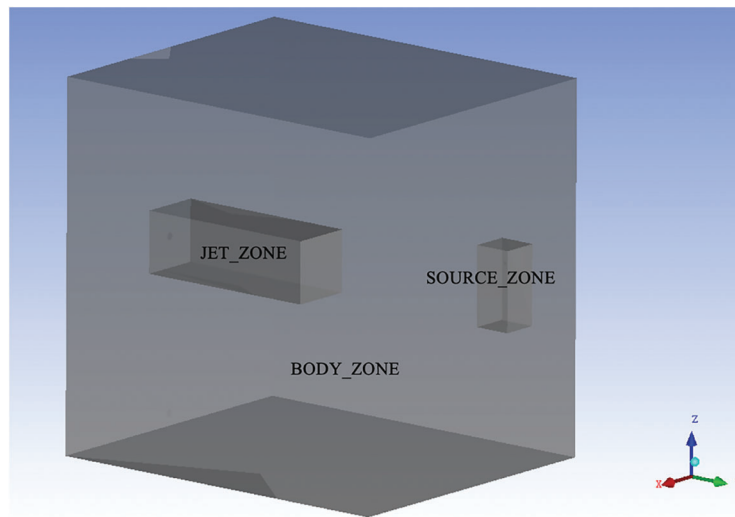


Figure 6: Subdivisions of the large space

The JET_ZONE was the area around the jet, which had a high velocity at the outlet and high gradient of velocity along the jet centerline and the radius of the jet cross-section. The SOURCE_ZONE is the area around the source. There were fine and high-quality mesh (all hexahedral) in this zone.

In the rest of the space, the velocity gradient and the contaminant gradient were both low, and the tetrahedral mesh was sufficient for this zone. The grids division can be seen in Fig. 7. Figs. 7a and 7b show the distribution of grids in parts JET_ZONE and SOURCE_ZONE, respectively.

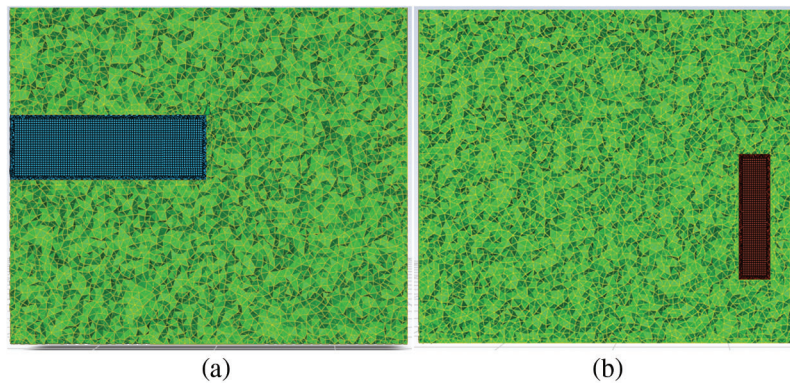


Figure 7: Grid division diagram

Four sets of grids were used to simulate the velocity field with the standard $k-\varepsilon$ model and standard wall function. The grid numbers were 1.0 million, 1.5 million, 2.0million and 2.5 million. Fig. 8 shows the comparison of the velocity field for different grid numbers under test line of $x = 2.5$ m, $y = 3$ m and $x = 2.5$ m, $y = 5$ m.

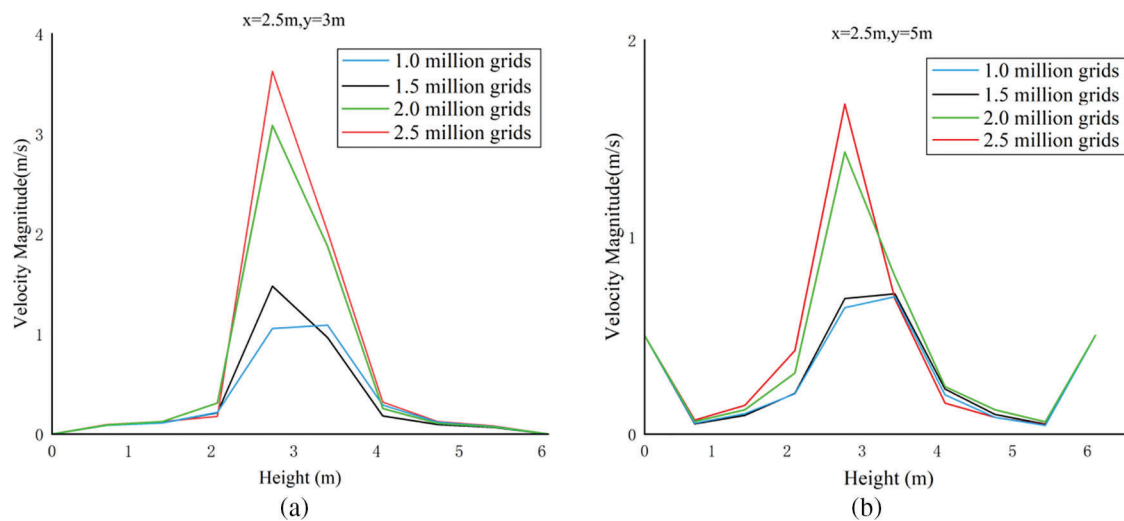


Figure 8: Comparison of velocity field for different grid numbers

As can be seen from Fig. 8, the overall trend of the velocity field of the four grid numbers are the same, indicating that the number of grids selected in this paper can meet the computational requirements. For 1.0 million grids and 1.5 million grids, due to the larger size of the grids, there are some differences in the results computed with the remaining two grids. The 2.0 million grid proved to be fine enough for the velocity field simulation. It was therefore used in the following simulations.

3.3 Turbulence Model

The turbulent Schmidt number is a necessary parameter used to calculate the turbulent diffusivity when simulation indoor gas dispersion; it is a fitting parameter that depends on the mean and turbulent characteristics of the flow field, the position and type of pollutant source, and so on. In RANS models,

the variables in the instantaneous Navier–Stokes equations are decomposed into the mean and fluctuating components. For the velocity components,

$$u_i = \bar{u}_i + u'_i \quad (2)$$

For pressure and other scalar quantities,

$$\varphi = \bar{\varphi} + \varphi' \quad (3)$$

Substituting expressions of this form for the flow variables into the instantaneous continuity and momentum equations and taking time (or ensemble) average (and dropping the overbar on the mean velocity, \bar{u}_i) yields the ensemble-averaged momentum equations. They can be written in Cartesian tensor form as follows [28,29]:

$$\frac{\partial \rho}{\partial t} + \frac{\partial}{\partial x_i}(\rho u_i) = 0 \quad (4)$$

$$\frac{\partial}{\partial t}(\rho u_i) + \frac{\partial}{\partial x_i}(\rho u_i u_j) = \frac{\partial p}{\partial x_i} + \frac{\partial}{\partial x_j} \left[\mu \left(\frac{\partial u_i}{\partial x_j} + \frac{\partial u_j}{\partial x_i} - \frac{2}{3} \delta_{ij} \frac{\partial u_l}{\partial x_l} \right) \right] + \frac{\partial}{\partial x_j} \left(-\rho \overline{u'_i u'_j} \right) \quad (5)$$

The two equations above are called RANS equations. The Reynolds stresses, $-\rho \overline{u'_i u'_j}$, must be modeled to close Eq. (5).

A common method employs the Boussinesq hypothesis to relate the Reynolds stresses to the mean velocity gradients:

$$-\rho \overline{u'_i u'_j} = \frac{\partial}{\partial t}(\rho u_i) + \frac{\partial}{\partial x_i}(\rho u_i u_j) = \mu_t \left(\frac{\partial u_i}{\partial x_j} + \frac{\partial u_j}{\partial x_i} \right) - \frac{2}{3} \delta_{ij} \left(\frac{\partial u_k}{\partial x_k} + \rho k \right) \quad (6)$$

To model the turbulent viscosity, μ_t , turbulence models are introduced into the governing equations. The most frequently used are the k - ε models, which introduce two more equations, namely the transport equation for kinetic energy k and the transport equation for its dissipation rate ε , which can be obtained from the following transport equations:

$$\frac{\partial}{\partial t}(\rho k) + \frac{\partial}{\partial x_i}(\rho k u_i) = \frac{\partial}{\partial x_j} \left[\left(\mu + \frac{\mu_t}{\sigma_k} \right) \frac{\partial k}{\partial x_j} \right] + G_k + G_b - \rho \varepsilon - Y_M + S_k \quad (7)$$

and

$$\frac{\partial}{\partial t}(\rho \varepsilon) + \frac{\partial}{\partial x_i}(\rho \varepsilon u_i) = \frac{\partial}{\partial x_j} \left[\left(\mu + \frac{\mu_t}{\sigma_\varepsilon} \right) \frac{\partial \varepsilon}{\partial x_j} \right] + C_{1\varepsilon} \frac{\varepsilon}{k} (G_k + C_{3\varepsilon} G_b) - C_{2\varepsilon} \rho \frac{\varepsilon^2}{k} + S_\varepsilon \quad (8)$$

The turbulent viscosity can be represented by k and ε :

$$\mu_t = \rho C_\mu \frac{k^2}{\varepsilon} \quad (9)$$

G_b is generation of turbulence kinetic energy due to buoyancy, the formula is $G_b = \beta g_i \frac{\mu_t}{Pr_t} \frac{\partial T}{\partial x_i}$, where Pr_t is the turbulent Prandtl number for energy, the default value of Pr_t is 0.85; G_k is generation of turbulence kinetic energy due to the mean velocity gradients, the formula is $G_k = -\rho \overline{u'_i u'_j} \frac{\partial u_j}{\partial x_i}$. Y_M is contribution of the fluctuating dilatation in compressible turbulence to the overall dissipation rate, this study defaults to incompressible fluids, which is ignored for this item. S_k and S_ε are user-defined source term, which are ignored in this study.

The differences among the various k - ε models concern the values for C_μ and the constants in the k equation and ε equation.

We adopted a standard wall function and ensured that most of the wall y star values lay in the region of 15–300.

3.4 Simulation Configurations

In the validation case, the air change rate for the space was 3 h^{-1} . For the contaminant source, the emission rate was 3 mL/s . The contaminant gas was SF_6 , an inorganic compound, is a colorless, odorless, non-toxic, non-flammable and stable gas at room temperature and pressure, with a density of 6.0886 kg/m^3 at 20°C and 0.1 MPa , about 5 times the density of air. For the choice of time step, choosing 5-s time step for a 40-s transient simulation makes the solution speed, convergence and accuracy better. The Sc_t was set to 0.4, 0.7, and 1, respectively.

For comparison, we conducted a set of simulations with high emission rates. The SF_6 was released at a rate of 265.5 mL/s while the air change rate for the space was still 3 h^{-1} .

Moreover, a set of simulations with high emission rates and light gas was also conducted. The emission rate was 265.5 mL/s , and the contaminant gas was hydrogen (H_2), is a colorless, odorless and highly flammable gas at room temperature and pressure, with a density of 0.089 g/L at 0°C and 101.325 kPa , which is only 1/14 of air and is the least dense gas known in the world.

4 Results and Discussion

4.1 Validation of the Simulation

In order to investigate which of standard k - ε model and realizable k - ε model predicts the velocity field more accurately, we conducted transient simulations of standard k - ε model and realizable k - ε model and compared them with the experimental data as shown in Fig. 9. Fig. 9 compares the vertical profiles of the velocity magnitudes for the standard k - ε model and realizable k - ε model with the experimental data. The turbulent intensities at the inlet were set to 40% for both models. The prediction results are similar and generally close to the experimental results. Fig. 9 shows the simulation data and experimental data on seven vertical lines, spatially distributed the same as the experiment measuring rigs.

The velocity profiles at the line which $x = 2.5 \text{ m}$, $y = 3 \text{ m}$ and the line which $x = 2.5 \text{ m}$, $y = 5 \text{ m}$ agree well with the experiment. For both the standard k - ε model and the realizable k - ε model, improving the intensity at the inlet can lower the velocity magnitude on the centreline of the jet. This effect is more notable for the standard k - ε model. The openings in the experiments are grilles, while in the model we simplified them to round openings of which the areas are equal to the effective area in the experiment. Improving the turbulent intensity can compensate for this simplification. When the turbulent intensity of the inlet is 40%, the realizable k - ε model shows a smaller decay on the jet, which is more in accordance with the experimental results.

For the measurement points at the line which $x = 0.5 \text{ m}$, $y = 3 \text{ m}$ and the line which $x = 4.5 \text{ m}$, $y = 3 \text{ m}$, the velocity magnitudes are underestimated by both the standard k - ε model and the realizable k - ε model. The effect of the turbulent intensity at the inlet is not notable outside the jet. For the measurement points at the line which $x = 0.5 \text{ m}$, $y = 1 \text{ m}$ and the line which $x = 4.5 \text{ m}$, $y = 1 \text{ m}$, the realizable k - ε model gives a higher prediction than the standard k - ε model. The realizable model fits better with the experimental data.

Generally, the realizable k - ε model and a turbulent intensity of 40% at the inlet predicts the velocity field most accurately.

Fig. 10 compares the simulated transient concentrations at several locations with the experimental data when Sc_t is set to the default of 0.7. For P1, P3, P6, P9, and P10, the simulation results fit the experimental data well. For P7, P8, P11, P12, P14, and P16, the predicted concentrations are higher than the experimental

results. The positions where the concentration is overestimated in Fig. 10 are also where the velocity is underestimated in Fig. 9, which means that the concentration is related to the local velocity. It also shows that the realizable k- ϵ model with the species transport model can predict the concentration distribution well.

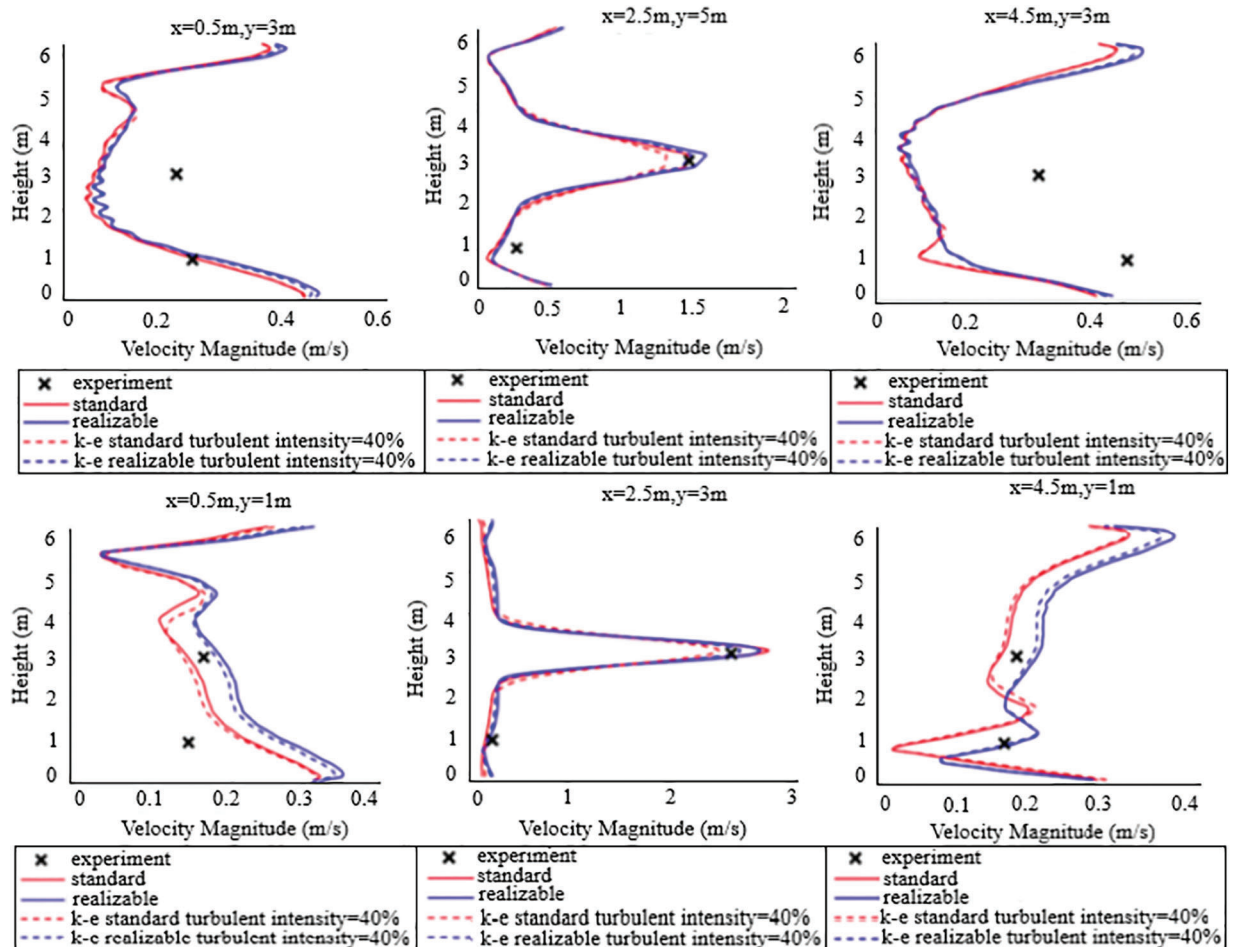


Figure 9: Vertical velocity profiles at different locations

4.2 Impact of Sc_c on Dimensionless Concentration Distribution

With the validated turbulence model and species transport model, we conducted three sets of simulations, as described in Section 3.4. As the emission rate changed in different simulation configurations, we needed a dimensionless concentration to judge the contaminant distribution. The dimensionless concentration C_{star} is defined as

$$C_{star} = \frac{C}{C_0} \quad (10)$$

$$C_0 = \frac{q}{Q_v} \quad (11)$$

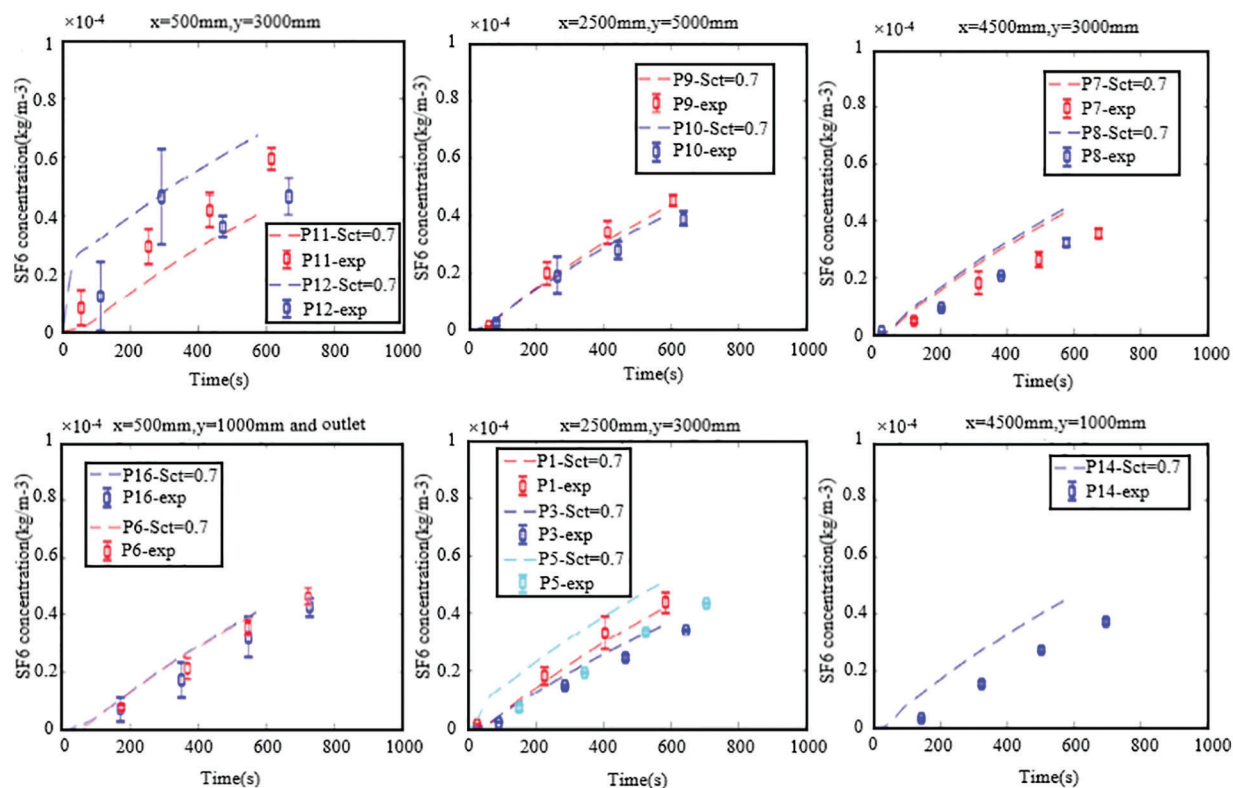


Figure 10: Transient concentration evolutions at different locations

The dimensionless concentration is used in this section to judge the effect of Sc_t on the concentration distribution.

4.2.1 Contaminant Source of SF₆ Released at 3 mL/s

Fig. 11 gives the dimensionless concentration at $X = 0.5$ m after 40 s of releasing SF₆ at 3 mL/s. In this set of simulations, since the contaminant emission rate was low, the gravity seemed not affect the dispersion of SF₆. The SF₆ was influenced more by the flow in the space and moved upward. The area of iso- C_{star} for each grade is the smallest when $Sc_t = 0.4$ and the largest when $Sc_t = 1$.

4.2.2 Contaminant Source of SF₆ Released at 265.5 mL/s

Fig. 12 gives the dimensionless concentration at $X = 0.5$ m after 40 s of releasing SF₆ at 265.5 mL/s. In this set of simulations, since the contaminant emission rate is high, the dispersion of SF₆ around the source was more influenced by the gravitational force and moved downward. The area of iso- C_{star} for each grade is the smallest when $Sc_t = 0.4$ and the largest when $Sc_t = 1$.

Comparing Figs. 11 and 12, one can see that, although the emission rate differs, the effect of Sc_t is identical: the increase of Sc_t accelerates the contaminant transportation.

4.2.3 Contaminant Source of H₂ Released at 265.5 mL/s

Fig. 13 gives the dimensionless concentration at $X = 0.5$ m after 40 s of releasing H₂ at 265.5 mL/s. In this set of simulations, the low density of H₂ took effect. The H₂ concentration around the source was more influenced by the buoyancy and moved downward. The area of iso- C_{star} for each grade is the largest when $Sc_t = 0.4$ and the smallest when $Sc_t = 1$. For H₂, the increase of Sc_t decelerates contaminant transportation. Comparing Figs. 12 and 13, we can conclude that different contaminant gases have different effects on the Sc_t , so it is not very rigorous to set it to a fixed value in the transient simulation.

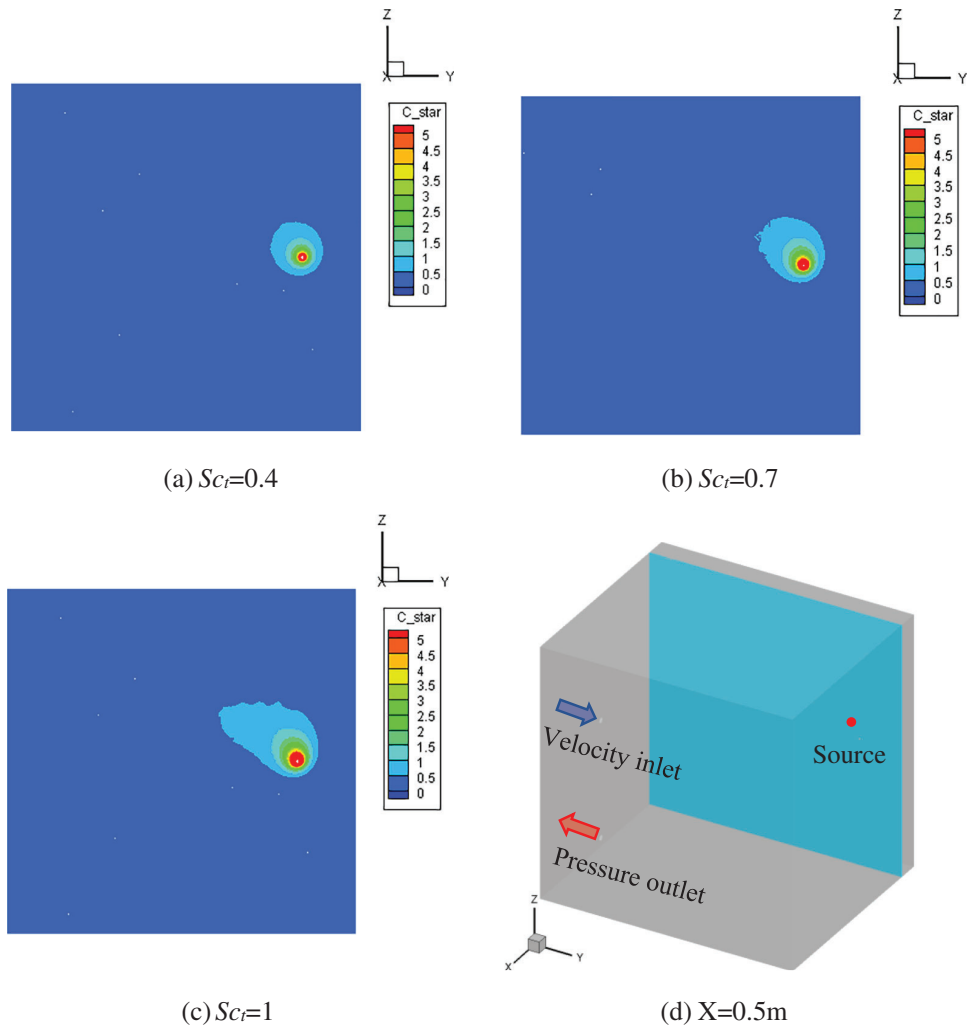


Figure 11: Dimensionless concentration at $X = 0.5$ m plane when sulfur hexafluoride has been released at low emission rate for 40 s

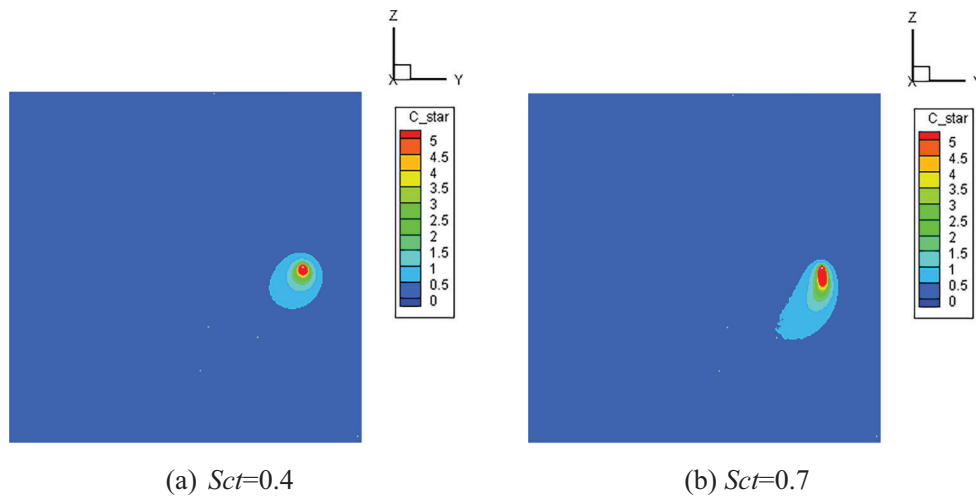


Figure 12: (Continued)

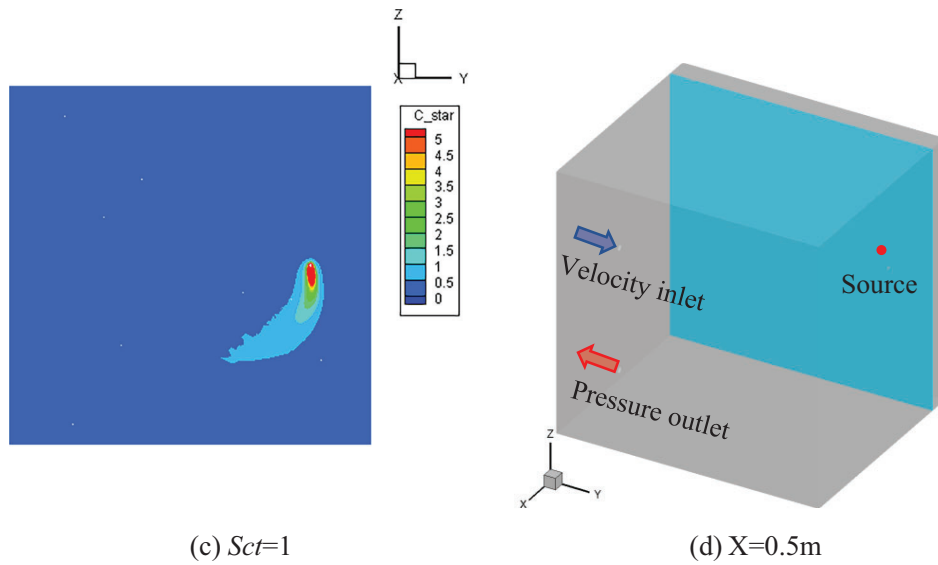


Figure 12: Dimensionless concentration at $X = 0.5$ m when sulfur hexafluoride has been released at a high emission rate for 40 s

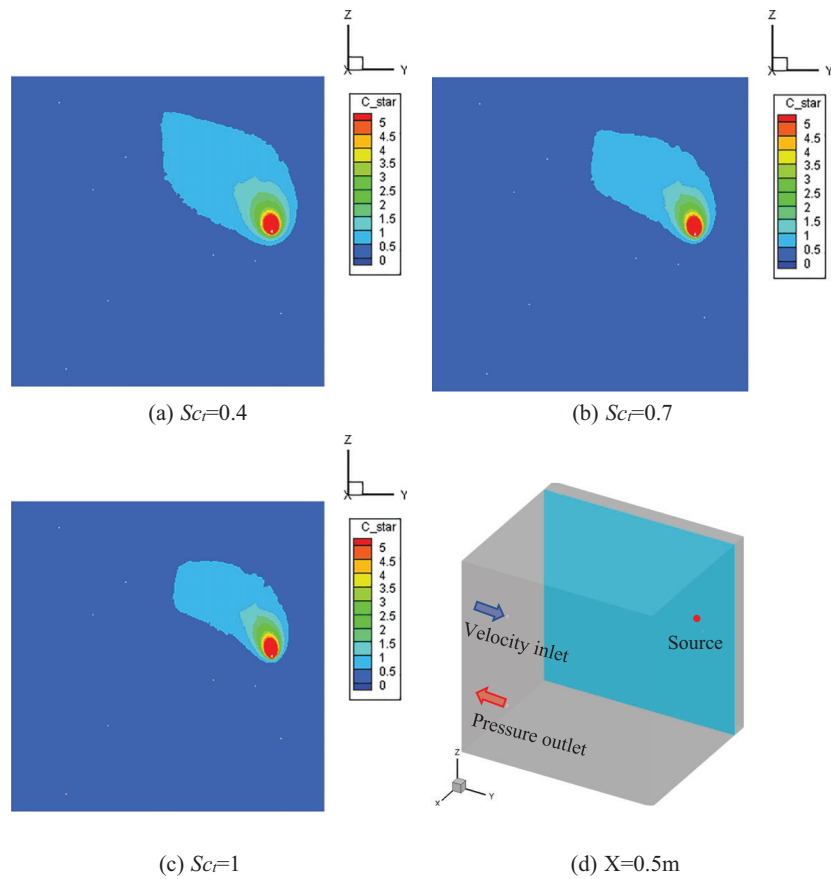


Figure 13: Dimensionless concentration at $X = 0.5$ m plane when hydrogen has been released at low emission rate for 40 s

In summary, we can find that the effect of Sc_t on gas dispersion is different for different densities of gases, for higher density gases such as SF₆, the gas dispersion rate is positively related to Sc_t ; on the contrary, for lower density gases such as H₂, the gas dispersion rate is negatively related to Sc_t . So for the indoor contaminant, the higher the density of the gas, we have to choose a lower Sc_t ; for the lower density of the gas, we have to choose a higher Sc_t .

It can be seen that Sc_t is important for gas pollutant diffusion simulation. A default value cannot fit every gas pollutant. More in-depth studies are needed on Sc_t for diffusion simulation of other different gases, even ultra-fine particulate matter and bio-aerosols, etc.

5 Conclusions

To study the influence of Schmidt number on contaminant gas dispersion, we adopted a validated CFD model, which include the realizable k- ϵ turbulent model and a turbulent intensity of 40% at the inlet, to predict flow field and concentration of contaminant gas. And following conclusions were obtained.

For SF₆ as the contaminant gas, the emission rate completely changed the concentration distribution. When the emission rate was low, the gravitational effect did not take place.

For both low and high emission rates, improving Sc_t accelerated the transportation of the SF₆.

For H₂ as the contaminant gas, improving Sc_t decelerated the transportation of the H₂, which is the opposite of the pattern for SF₆. So for the research subjects SF₆ and H₂ chosen in this paper, SF₆ is more suitable for $Sc_t = 0.4$, choosing the smallest possible Sc_t ; H₂ is more suitable for $Sc_t = 1$, choosing the largest possible Sc_t . The Sc_t applicable to the diffusion simulation of different gases is worthy of further study.

Acknowledgement: None.

Funding Statement: This research were funded by the National Natural Science Foundation of China and the Machinery Industry Innovation Platform Construction Project of China Machinery Industry Federation, Grant Numbers 52378103 and 2019SA-10-07.

Author Contributions: The authors confirm contribution to the paper as follows: study conception and design: F.W. and Q.Z.; data collection: J.Z.; analysis and interpretation of results: X.W. and Y.L.; draft manuscript preparation: Q.M. and F.W. All authors reviewed the results and approved the final version of the manuscript.

Availability of Data and Materials: The data used in the study are available from corresponding author, please contact zhangqianru@usst.edu.cn.

Conflicts of Interest: The authors declare that they have no conflicts of interest to report regarding the present study.

References

1. Mazzola, T., Hanna, S., Chang, J. (2021). Results of comparisons of the predictions of 17 dense gas dispersion models with observations from the Jack Rabbit II chlorine field experiment. *Atmospheric Environment*, 244, 117887. <https://doi.org/10.1016/j.atmosenv.2020.117887>
2. He, J. X., Liu, L., Li, A. G., Ma, Y., Zhou, D. M. (2021). A dense gas dispersion model based on revised meteorological parameters and its performance evaluation. *Atmospheric Environment*, 244, 117953. <https://doi.org/10.1016/j.atmosenv.2020.117953>
3. Turner, D. B. (2020). *Workbook of atmospheric dispersion estimates: An introduction to dispersion modeling*. USA: CRC Press.
4. Weil, J. C., Alessandrini, S. (2023). The integral dense-gas dispersion model (IDDM) and comparison with Jack Rabbit II data. *Atmospheric Environment*, 296, 119563. <https://doi.org/10.1016/j.atmosenv.2022.119563>

5. Siddiqui, M., Jayanti, S., Swaminathan, T. (2012). CFD analysis of dense gas dispersion in indoor environment for risk assessment and risk mitigation. *Journal of Hazardous Materials*, 209, 177–185.
6. Rutkowski, D. R., Roldán-Alzate, A., Johnson, K. M. (2021). Enhancement of cerebrovascular 4D flow MRI velocity fields using machine learning and computational fluid dynamics simulation data. *Scientific Reports*, 11, 10240. <https://doi.org/10.1038/s41598-021-89636-z>
7. Spalding, D. (1971). Concentration fluctuations in a round turbulent free jet. *Chemical Engineering Science*, 26, 95–107.
8. Bady, M., Kato, S., Huang, H. (2008). Towards the application of indoor ventilation efficiency indices to evaluate the air quality of urban areas. *Building and Environment*, 43(12), 1991–2004. <https://doi.org/10.1016/j.buildenv.2007.11.013>
9. Tahmooreesi, S., Ahmadyar, D. (2021). Effects of turbulent Schmidt number on CFD simulation of 45° inclined negatively buoyant jets. *Environmental Fluid Mechanics*, 21, 39–62. <https://doi.org/10.1007/s10652-020-09762-6>
10. Balestrin, E., Souza, S. M. A. G. U. D., Valle, J. A. B. (2021). Sensitivity of the turbulent Schmidt number and the turbulence models to simulate catalytic and photocatalytic processes with surface reaction limited by mass transfer. *Chemical Engineering Research and Design*, 170, 90–106. <https://doi.org/10.1016/j.chemd.2021.03.035>
11. Blázquez, J. L. F., Maestre, I. R. (2023). Experimental adjustment of the turbulent Schmidt number to model the evaporation rate of swimming pools in CFD programmes. *Case Studies in Thermal Engineering*, 41, 102665. <https://doi.org/10.1016/j.csite.2022.102665>
12. Abe, S., Studer, E., Ishigaki, M. (2020). Density stratification breakup by a vertical jet: Experimental and numerical investigation on the effect of dynamic change of turbulent schmidt number. *Nuclear Engineering and Design*, 368, 110785. <https://doi.org/10.1016/j.nucengdes.2020.110785>
13. Chowdhury, M. N., Aziz, S. (2021). Effects of turbulence modeling and turbulent Schmidt number on supersonic mixing simulations. *ASME International Mechanical Engineering Congress and Exposition*. <https://doi.org/10.1115/IMECE2021-69458>
14. Koeltzsch, K. (2000). The height dependence of the turbulent Schmidt number within the boundary layer. *Atmospheric Environment*, 34(7), 1147–1151.
15. Tominaga, Y., Stathopoulos, T. (2007). Turbulent Schmidt numbers for CFD analysis with various types of flowfield. *Atmospheric Environment*, 41(37), 8091–8099.
16. He, G., Guo, Y., Hsu, A. T. (1999). The effect of Schmidt number on turbulent scalar mixing in a jet-in-crossflow. *International Journal of Heat and Mass Transfer*, 42(20), 3727–3738.
17. Kamotani, Y., Greber, I. (1972). Experiments on a turbulent jet in a cross flow. *AIAA Journal*, 10(11), 1425–1429.
18. Gromke, C., Blocken, B. (2015). Influence of avenue-trees on air quality at the urban neighborhood scale. Part I: Quality assurance studies and turbulent Schmidt number analysis for RANS CFD simulations. *Environmental Pollution*, 196, 214–223. <https://doi.org/10.1016/j.envpol.2014.10.016>
19. Nagaosa, R. S. (2014). A new numerical formulation of gas leakage and spread into a residential space in terms of hazard analysis. *Journal of Hazardous Materials*, 271, 266–274.
20. Cao, S. J., Meyers, J. (2013). Influence of turbulent boundary conditions on RANS simulations of pollutant dispersion in mechanically ventilated enclosures with transitional slot Reynolds number. *Building and Environment*, 59, 397–407.
21. Dong, L. X., Zuo, H. C., Hu, L., Yang, B., Li, L. C. et al. (2017). Simulation of heavy gas dispersion in a large indoor space using CFD model. *Journal of Loss Prevention in the Process Industries*, 46, 1–12. <https://doi.org/10.1016/j.jip.2017.01.012>
22. Marquardt, P., Klaas, M., Schröder, W. (2020). Experimental investigation of the turbulent Schmidt number in supersonic film cooling with shock interaction. *Experiments in Fluids*, 61, 160. <https://doi.org/10.1007/s00348-020-02983-x>
23. Shi, Z., Chen, J., Chen, Q. Y. (2016). On the turbulence models and turbulent Schmidt number in simulating stratified flows. *Journal of Building Performance Simulation*, 9(2), 134–148.
24. Li, F., Liu, J. J., Ren, J. L., Cao, X. D. (2018). Predicting contaminant dispersion using modified turbulent Schmidt numbers from different vortex structures. *Building and Environment*, 130, 120–127.

25. Zhang, Q., Zhang, X., Ye, W., Liu, L., Nielsen, P. V. (2018). Experimental study of dense gas contaminant transport characteristics in a large space chamber. *Building and Environment*, 138, 98–105.
26. Deng, B. C., Shin, Y. J., Lu, L., Zhang, Z. Q., Karniadakis, G. E. (2022). Approximation rates of DeepONets for learning operators arising from advection-diffusion equations. *Neural Networks*, 153, 411–426. <https://doi.org/10.1016/j.neunet.2022.06.019>
27. Jena, S. R., Gebremedhin, G. S. (2021). Computational technique for heat and advection—diffusion equations. *Soft Computing*, 25, 11139–11150. <https://doi.org/10.1007/s00500-021-05859-2>
28. Fluent, A. (2023). *2023R1 theory guide*. USA: Ansys Inc.
29. Fluent, A. (2023). *2023R1 user's guide*. USA: Ansys Inc.